Visualizing Model Data Using a Fast Approximation of a Radiative Transfer Model

VALLIAPPA LAKSHMANAN

Cooperative Institute of Mesoscale Meteorological Studies, University of Oklahoma, and National Oceanic and Atmospheric Administration/National Severe Storms Laboratory, Norman, Oklahoma

ROBERT RABIN

National Oceanic and Atmospheric Administration/National Severe Storms Laboratory, Norman, Oklahoma

JASON OTKIN

Space Science and Engineering Center, University of Wisconsin—Madison, Madison, Wisconsin

JOHN S. KAIN

National Oceanic and Atmospheric Administration/National Severe Storms Laboratory, Norman, Oklahoma

SCOTT DEMBEK

Cooperative Institute of Mesoscale Meteorological Studies, University of Oklahoma, and National Oceanic and Atmospheric Administration/National Severe Storms Laboratory, Norman, Oklahoma

(Manuscript received 3 January 2011, in final form 21 December 2011)

ABSTRACT

Visualizing model forecasts using simulated satellite imagery has proven very useful because the depiction of forecasts using cloud imagery can provide inferences about meteorological scenarios and physical processes that are not characterized well by depictions of those forecasts using radar reflectivity. A forward radiative transfer model is capable of providing such a visible-channel depiction of numerical weather prediction model output, but present-day forward models are too slow to run routinely on operational model forecasts.

It is demonstrated that it is possible to approximate the radiative transfer model using a universal approximator whose parameters can be determined by fitting the output of the forward model to inputs derived from the raw output from the prediction model. The resulting approximation is very close to the result derived from the complex radiative transfer model and has the advantage that it can be computed in a small fraction of the time required by the forward model. This approximation is carried out on model forecasts to demonstrate its utility as a visualization and forecasting tool.

1. Introduction

Precipitation forecasts from numerical weather prediction (NWP) models have traditionally been presented to forecasters as accumulated depth over specified time intervals (e.g., 6 h). Guidance regarding clouds has generally been lacking, aside from postprocessed statistics about general cloud properties such as cloud cover (e.g., Jakob 1999; Teixeira and Hogan 2002). Part of the reason for this rather ambiguous presentation of clouds and precipitation is that many aspects of these features have been parameterized in forecast models, rather than explicitly represented on the model grid (e.g., Sundqvist et al. 1989; Janjic 1990). However, in recent years, increases in computer power have allowed operational NWP centers to increase spatial resolution and explicitly resolve more key processes, such as deep precipitating convection, which were previously parameterized (e.g., Weiss et al. 2008; Dixon et al. 2009). This transition has allowed for the development of new ways to visualize explicit forecasts for clouds and precipitation.

Most of this visualization work has focused on precipitation. Explicit precipitation output predicted by NWP models with grid spacing on the order of several

Corresponding author address: V. Lakshmanan, 120 David L. Boren Blvd., Norman, OK 73072.
E-mail: lakshman@ou.edu

DOI: 10.1175/JTECH-D-11-00007.1

kilometers is now commonly viewed as a simulated reflectivity product (e.g., Kain et al. 2008). This product is particularly revealing not so much because it depicts the instantaneous precipitation rate, but because the patterns formed by simulated reflectivity fields can be used to infer a multitude of circulations, processes, and configurations associated with precipitating weather systems (Koch et al. 2005). Simulated reflectivity provides useful guidance for forecasters (e.g., Weisman et al. 2008) and has been used for model validation in numerous arenas, such as the National Oceanic and Atmospheric Administration (NOAA) Hazardous Weather Test bed (HWT; e.g., Kain et al. 2010b).

Visualization of clouds, in the form of simulated satellite imagery, can also provide unique information about NWP model output (e.g., Otkin and Greenwald 2008; Otkin et al. 2009). Although synthetic satellite imagery has received less attention in the weather forecasting community, it may ultimately prove to be more valuable than simulated reflectivity because most clouds are nonprecipitating. Thus, cloud imagery can provide inferences about physical processes not associated with precipitation (e.g., Feltz et al. 2009) and/or processes that could allow forecasters to anticipate better the development of precipitation. Synthetic satellite imagery has also proven to be useful in the NOAA HWT in recent years (Clark et al. 2012).

One way to calculate the reflectance for the Geostationary Operational Environmental Satellite (GOES) 0.65-μm visible channel is to use a complex forward modeling system such as the Successive Order of Interaction (SOI) model developed by Heidinger et al. (2006) wherein gas optical depths are computed for each model layer and absorption and scattering properties are applied to each hydrometeor species predicted by the model microphysics parameterization scheme.

Even with the recent development of fast forward radiative transfer models, computing simulated satellite observations, particularly those for visible channels, remains a very time-consuming task. For instance, approximately 13 h are required to compute GOES 0.65-μm reflectances for a single output time for the high-resolution, large-domain model configuration used for this study (1200 $\times$ 800 horizontal grid points and 35 vertical levels) using the SOI model. Though the wall-clock time could be substantially reduced by using multiple processors, the overall high computational cost remains and renders the real-time generation of such observations difficult using present computational resources. Because of this, it is useful to explore other means to generate simulated visible satellite imagery in real time. In this paper, we suggest the approach of creating an approximation of the forward model using a parametric approximation.

Neural networks (NNs) are a nonlinear statistical modeling tool that were motivated by analogies to biological neural networks. Neural networks have enjoyed widespread use in meteorological applications, ranging from prediction of rainfall amounts (Venkatesan et al. 1997), and diagnosing tornado probability (Marzban and Stumpf 1996) to quality control (Lakshmanan et al. 2007). However, all these uses of neural networks are data driven, aiming to predict a desired value based on inputs whose individual impacts are unknown. Our use of neural networks is as an approximating mechanism, to approximate a known function that is too complex to compute. In other words, we know the exact impact of each input variable, but the transfer functions are too time consuming to compute. The use of a neural network as a functional approximation is rarer in meteorological applications, but has been explored before, notably by Krasnopolsky et al. (2008).

We employed a neural network of the form:

$$y = \sum_{j=1}^{M} w_j h\left(\sum_{i=0}^{d} w_{ji} x_i\right), \tag{1}$$

where y is the output of the NN and the x_i are the inputs (there are d ''true'' inputs with x_0 fixed to be a constant value of 1). The w's are referred to as the weights and the ''transfer function'' $h(x)$ is given by

$$h(x) = \frac{1}{1 + e^{-x}}. \tag{2}$$

Each layer of transfer functions in the neural network adds a ''hidden layer'' (i.e., a set of transformations whose inputs and outputs are not the inputs and output of the equation as a whole). In this case, the input of the hidden layer is a weighted combination of the input values x_i. The output y of the NN is a weighted combination of the results of the transfer function at each of the M hidden nodes. Neural networks of this form are capable of approximating any continuous functional mapping to arbitrary accuracy and are therefore suitable for use as universal approximators (Bishop 1995).

A natural question that arises is why we need to approximate the forward model using the NN, rather than have the NN approximate the observed visible field directly. There are several problems with training a NN to estimate visible channel reflectance from model fields, but the key problem is that model forecasts (and even analysis fields) suffer from displacement and distortion errors. In addition, some clouds visible on satellite imagery may not be depicted in the model and vice versa. Finally, the satellite visible imagery is influenced by surface reflectance, darkening due to sun angle, parallax

errors, shadows, etc., all of which would have to be accounted for when training a NN to predict the observed value. Using a forward model where some of these effects can be switched off provides more control when training a NN.

2. Approximating the forward model

To approximate the forward model, a small, but diverse, set of numerical model data was selected as representative input. The objective is to train the neural network to approximate the behavior of the forward model on this dataset. At each 2D pixel of the model grid, data values from various model fields (mixing ratios, temperature, pressure, etc.) were used as inputs to a neural network. The goal of training was for the resulting neural network to yield the best possible approximation of what the forward model does on the dataset. If the training dataset is indeed representative, then the neural network approximation can be used in lieu of the computationally more expensive forward model on real-time data to generate forecasts of visible imagery.

It should be noted that because the neural network is an approximation of the forward model, it suffers from all the limitations of the forward model. For example, because present-day forward models are not capable of depicting cloud shadows, the NN approximation is also not capable of depicting cloud shadows.

a. Training dataset

The optimization (or ''training'') process for the NN consists of finding the best set of w_{ij} [in Eq. (1)] that will allow the output of the neural network to approximate the behavior of the radiative transfer forward model on the dataset. In other words, the target value y_t is obtained from the radiative transfer model and the input x_i are obtained from the NWP model forecast. The NN training process consists of determining the weights w_{ij} at which the square error computed over all the pixels of the training dataset [i.e., $\sum(y_t - y)^2$] is minimum.

The input dataset consisted of outputs from a Weather Research and Forecasting (WRF; Skamarock et al. 2005) model that is run routinely at the National Severe Storms Laboratory (NSSL), hereafter the NSSL-WRF (Kain et al. 2010a). The NSSL-WRF has 4-km horizontal grid spacing (grid size of 1200 × 800), 35 vertical levels, and a time step of 24 s. It uses the WRF Single-Moment 6-Class Microphysics scheme (WSM6) of Hong and Lim (2006). Initial and lateral boundary conditions are obtained from the North American model (Rogers et al. 2009).

The input dataset consisted of NSSL-WRF model forecasts for 1800–2300 UTC in 1-h increments on 3 April 1974, 1 July 2009, and 12–16 August 2009 (excluding 15 August 2009). At that time, the NSSL-WRF domain was somewhat smaller, covering the eastern two-thirds of the continental United States with 980 × 750 grid points. These model forecasts were provided to the forward model and the resulting visible channel reflectance values stored for each grid point at each time period. Because these datasets cover a wide area, this dataset captures a wide variety of weather situations.

One problem is that even with just six days of data, the representative training sets are incredibly large. We used data from 36 output times in order to train the model. Thus, the size of the input is about 26.5 million patterns (there is one pattern corresponding to every NSSL-WRF surface grid point). The model fields are numerous as well. Fourteen 3D fields such as temperature and perturbation geopotential are produced at every time step and for each of these fields, one would have to consider 35 vertical slices. In addition, there are 67 2D fields such as precipitation and soil moisture. Using all of the possible inputs would result in a training set that is about 15 billion points, a rather unrealistic option. Hence, we reduced the number of inputs by vertically integrating some of the 3D fields and choosing the input parameters based on the variables considered by the radiative transfer model and how these variables were employed within it.

In the forward model of Heidinger et al. (2006), gas optical depths are computed for each NSSL-WRF model layer using a lookup table containing layer atmospheric transmittances computed using line-by-line calculations. Ice cloud absorption and scattering properties, such as extinction efficiency, single scatter albedo, and full scattering phase function obtained from the work of Baum et al. (2005) are subsequently applied to each frozen (i.e., cloud ice, snow, and graupel) hydrometeor species predicted by the WRF model microphysics parameterization scheme. A lookup table based on Lorenz–Mie calculations (for the scattering of electromagnetic radiation) is used to assign the properties for the liquid (cloud water and rainwater) species. Visible cloud optical depths are calculated separately for the liquid and frozen hydrometeor species following the work of Han et al. (1995) and Heymsfield et al. (2003), respectively. Surface albedo and emissivity are obtained for land grid points using the Filled Land Surface Albedo Product dataset developed by the Moderate Resolution Imaging Spectroradiometer (MODIS) atmospheric science team (http://modis-atmos.gsfc.nasa.gov/ALBEDO/index.html). Over water surfaces, changes in reflectance due to waves and sun glint are considered using the model developed by Sayer et al.

(2010). Finally, the simulated skin temperature and atmospheric temperature profiles along with the layer gas optical depths and cloud scattering properties are input into the SOI forward radiative transfer model (Heidinger et al. 2006), which is used to compute the simulated visible reflectances. Readers interested in the details of the radiative transfer model are referred to Heidinger et al. (2006)—for the purposes of this paper, it is enough to understand that the radiative transfer model is computationally too intensive to carry out in real time.

The neural network is expected to approximate all these computations by the universal approximator shown in Eq. (1), except for the following modifications. Usually, the forward model takes the sun angle into account in order to darken the visible image appropriately. Since our goal is to create a synthetic visible field for the purpose of visualizing the model microphysics, darkening the image is inappropriate—there is no reason why one should not be able to visualize the model at night. Therefore, the forward model was modified to produce images with a fixed sun angle corresponding to local noon at all model output times. Another change that was made to the output of the forward model was to subtract out the surface albedo because a forecaster is interested in visualizing the cloud albedo and there is no need, in a synthetic field, to contaminate it with reflectance from the earth's surface.

Finally, all clear grid points (i.e., pixels where the mixing ratios of cloud water, cloud ice, and snow were all zero) were removed from the training set as, according to the numerical model, there would be no cloud cover whatsoever at that point. In the output of the neural network when run on operational NSSL-WRF model forecasts, such points were assigned a visible reflectance value of zero.

From the NSSL-WRF model layers, the following variables were used to train the approximation to the forward model:

1) qvapor, qcloud, qrain, qice, qsnow, and qgraup, which are the mixing ratios (kg kg^{-1}) of water vapor, cloud water, rain, cloud ice, snow, and graupel, respectively. These quantities that are available at every model layer were vertically integrated by weighting each layer's value with the thickness of that model layer in meters.
2) qvapor, qcloud, qrain, qice, qsnow, and qgraup (as above, but using only the top 17 model layers for the vertical integration).
3) qvapor, qcloud, qrain, qice, qsnow, and qgraup (vertically integrated by weighting each layer's value by *pressure*/*temperature* instead of by the thickness of the layer).

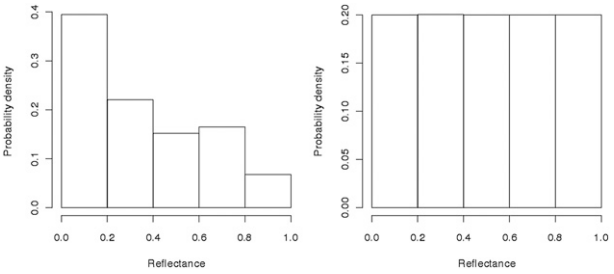

FIG. 1. Effect of histogram equalization. (left) Histogram of pixel brightness values based on the NSSL-WRF inputs. (right) Histogram of pixel brightness after randomized resampling.

4) Minimum temperature, height of minimum temperature.
5) Skin surface temperature (TSK).
6) Wind speed.

It may appear surprising that full vertical profiles of mixing ratios are provided to the neural network and not merely the characteristics of the uppermost cloud layer. It is necessary to use vertical profiles of temperature, humidity (i.e., water vapor mixing ratio), and cloud hydrometeor characteristics such as mixing ratio and effective particle diameter, in a forward radiative transfer model since all of these fields affect the top of atmosphere radiance, even for visible wavelengths. The common belief that a visible imager cannot see below the cloud top is inaccurate since this is dependent on the optical depth of the cloud. For example, a visible imager will also see the surface in the presence of semitransparent clouds such as cirrus.

b. Histogram equalization and downsampling

For the NSSL-WRF output on just these six days, there were a total of nearly 5 million grid points for which one of qcloud, qice, and qsnow was nonzero. A histogram of the visible reflectance values (Fig. 1) indicated that the majority of these values were low values. These aspects of the training dataset pose two problems: first, training directly with the original dataset would cause a machine intelligence algorithm to focus on getting low visible reflectance values right at the expense of the far less frequent high reflectance values. This is, of course, unsuitable behavior. To use a visible field to visualize a model field, it is critical to get the higher visible reflectance values right—the low values are not quite as important. Second, five million data points is far too many for most machine intelligence or statistical software to handle on the type of computers (workstations with 4 GB of RAM) that we had on hand to do the training.

To address these issues, we carried out a process of histogram equalization and downsampling. We downsampled the nearly 5 million point dataset to a fifth of its

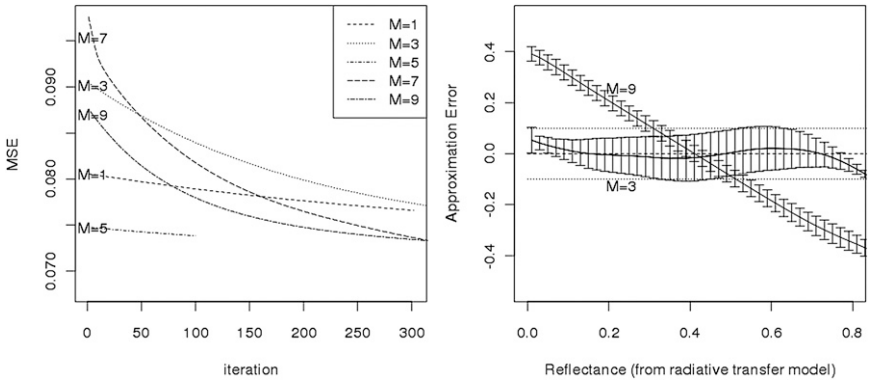

FIG. 2. Effect of the number of hidden nodes (M) on the approximation error. (left) The reduction in mean square error (MSE) during NN training. In general, more hidden nodes lead to lower MSEs. (right) Approximation error as it varies by reflectance. Using three hidden nodes has the property that the bias is within 0.1 for all reflectances.

size. These million grid points were obtained by randomly selecting grid points from the original dataset where the probability that a grid point was selected depended on its brightness value. Thus, grid points with a low brightness value had a lower probability of being selected, while grid points with a high brightness value were more likely to be selected. The likelihood of a grid point with brightness value b being selected depends on r, the repeat ratio, given by

$$r = nS/P(b), \tag{3}$$

where n is the number of nonzero bins in the histogram, S is the subsampling ratio (0.2 to reduce the dataset from 5 million to 1 million points), and $P(b)$ is the probability density of that brightness value (read out from the histogram in Fig. 1). If the r is, say 0.3, the grid point is selected with a probability of 0.3. This is achieved by generating a random number uniformly distributed in the range [0–1] and selecting the point if the random number is below 0.3. If the r is 2.3, the grid point is selected twice and a third time with a probability of 0.3. To avoid overfitting extremely rare values, the repeat ratio was capped at 5. The subsampling ratio of 0.2 was chosen because 1 million points was the hardware and software limit of our system. The repeat ratio was capped at 5 arbitrarily; any number of the same order of magnitude would have worked.

After histogram equalization and subsampling, the resulting dataset of approximately 1 million grid points had the frequency distribution shown in histogram on the right in Fig. 1.

c. Neural network training

A neural network with 31 input variables and 3 hidden nodes [i.e., in Eq. (1), $d = 31$ and $M = 3$] was trained on 1.01 million points selected through histogram equalization and randomized subsampling from a dataset consisting of 36 time steps from 6 days of NSSL-WRF model runs. We experimented with increasing the number of hidden nodes (see Fig. 2). While increasing the number of hidden nodes resulted in a lower mean square error in the approximation, this was subject to the classic bias-variance trade-off. Thus, as shown in the second panel of Fig. 2, using nine hidden nodes would result in a larger bias, but a lower variance. We chose to use the neural network with three hidden nodes because it has the nice property of having nearly all errors bounded within 0.1 (the dotted horizontal lines), while having only a slightly higher mean square error than the nine-node network (0.08 vs 0.075). The approximation error ($y - y_t$) is dimensionless and on the same scale as visible reflectance (0–1).

An example of the output of the forward model (run on NSSL-WRF model output valid at 2000 UTC 13 Aug 2009) and the corresponding NN approximation are shown in Fig. 3. Data from 13 Aug 2009 were part of the training datasets. The bottom panels of Fig. 3 show the output of the radiative transfer model and the NN approximation on NSSL-WRF forecast valid at 1800 UTC 28 Aug 2009. This is a dataset that was not used in creating the approximation (i.e., it was an independent test dataset). The first thing to note is that there are anticipated differences—the simulated imagery does not depict the land in areas where there is no cloud cover. Beyond that, the differences between the two images are only slight—some clouds appear brighter and others a little darker, but the cloud structure is faithfully represented in the approximation.

Magnitude differences between the output of the radiative transfer model and the NN approximation over the entire training dataset are shown in second panel of

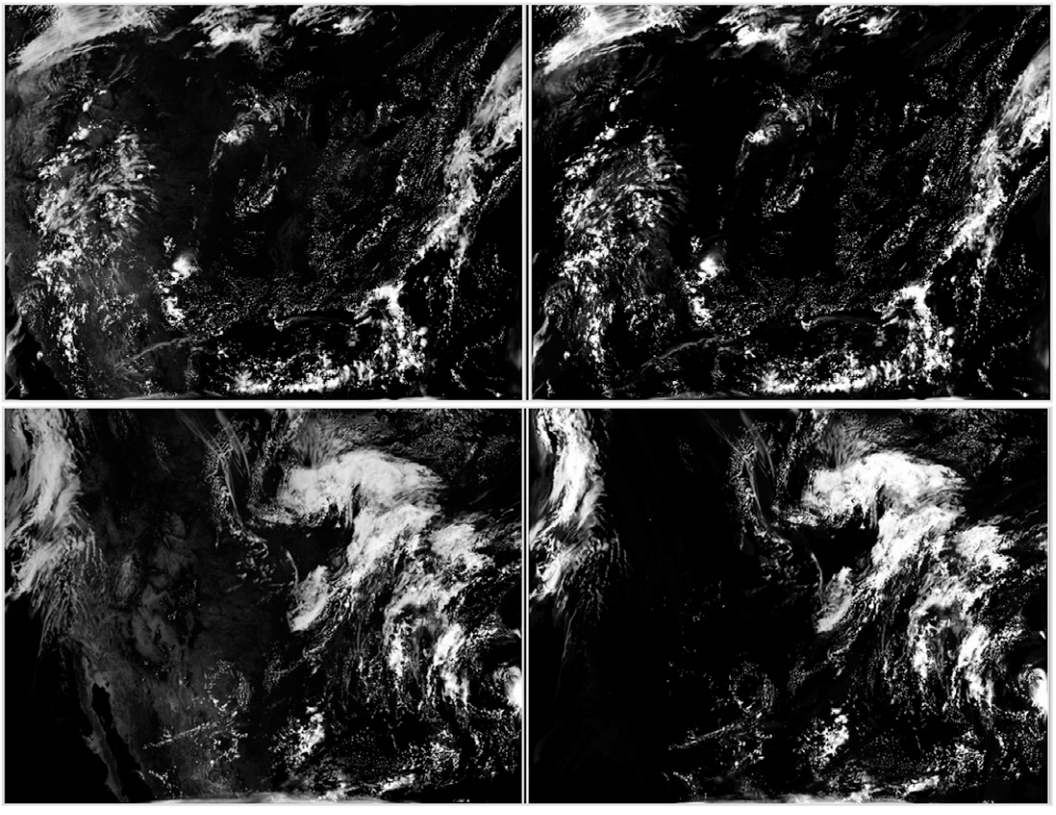

FIG. 3. (top left) Output of forward model run on NSSL-WRF model output valid at 2000 UTC 13 Aug 2009. (top right) Output of approximate model run on the same NSSL-WRF model variables. (bottom) As in (top), but on NSSL-WRF forecast valid at 1800 UTC 28 Aug 2009. Over the CONUS, on both days, both the forward model and the approximation depict the same clouds.

Fig. 2. This analysis of errors was carried out over the original 5 million points in the training dataset (i.e., before histogram equalization and downsampling). Looking at the graph for $M = 3$, it can be seen that the approximation errors are small and that the bias varies as a function of the true reflectance (i.e., reflectance value from the radiative transfer model). At very low values, below about 0.2, the approximation overestimates the reflectance (since the mean value of the approximation error, $y - y_t$, is greater than zero in this interval). At moderate values of reflectance, between about 0.2 and 0.5, the approximation tends to be an underestimate. At somewhat higher reflectance values, between about 0.5 and 0.7, the approximation is again an overestimate—it is these clouds that appear brighter in the simulated imagery in Fig. 3. Finally, the approximation underestimates extremely high values (reflectances above 0.7). We would like to caution that this graph should not be overanalyzed—the error magnitudes are almost all below 0.1 (shown by dotted horizontal lines). The error bars in the graph represent one standard deviation. Any biases that are present in the approximation are very small.

3. Visualization

The visible imagery are produced once a day at hourly intervals using input from the NSSL-WRF forecast microphysical data. Once the forecast has completed (approximately 4 h from the initialization time, 0000 UTC), the visible images are produced within 5 min on a single workstation. The full forward model, on the other hand, would have required a few hours computation time to run on a cluster of workstations.

Output of the visible imagery is made available for viewing on the web (http://www.nssl.noaa.gov/users/rabin/public_html/vis_wrf/) with options of two background fields: clear-sky surface albedo, and normalized difference vegetation index (NDVI).

The surface albedo is provided by the radiative transfer forward model of (Heidinger et al. 2006) and is based on solar elevation angles from August 2009. The NDVI data are produced from a 14-day composite of NOAA Advanced Very High Resolution Radiometer (AVHRR) data by the U.S. Geological Survey (USGS) Earth Resources Observation and Science (EROS) data

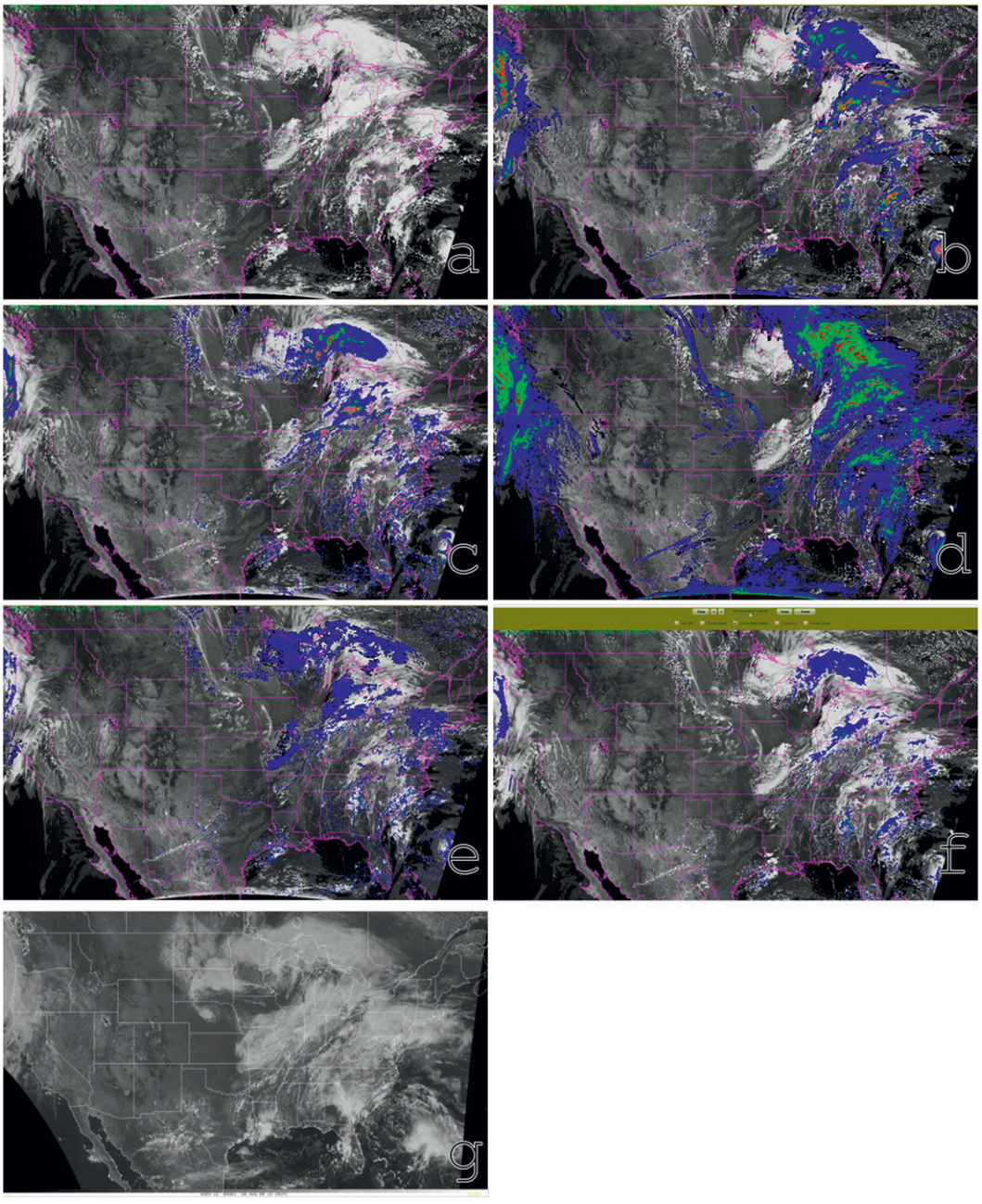

FIG. 4. The 18-h forecast valid at 1800 UTC 28 Aug 2009. Relative values of superimposed quantities (kg m^{-3}) increase from blue to green to red. (a) Visible image for 1800 UTC 28 Aug 2009 simulated using the NN approximation. (b) As in (a), but with vertically integrated cloud snow content superimposed. (c) As in (a), but with 1-h accumulated precipitation superimposed. (d) As in (a), but with the vertically integrated cloud ice content superimposed. (e) As in (a), but with the vertically integrated cloud water content superimposed. (f) As in (a), but with the vertically integrated cloud rainwater content superimposed. (g) Observed *GOES-12* visible satellite image at 1815 UTC 28 Aug 2009.

center. The data currently used as the background for the visible imagery are typical of summer. The NDVI image is color enhanced to represent the relative ''greenness'' of the surface.

There is also an option to display microphysical quantities from the forecast model as overlays on the visible imagery; vertically integrated cloud liquid water, rainwater, ice, snow, and forecast precipitation accumulated in

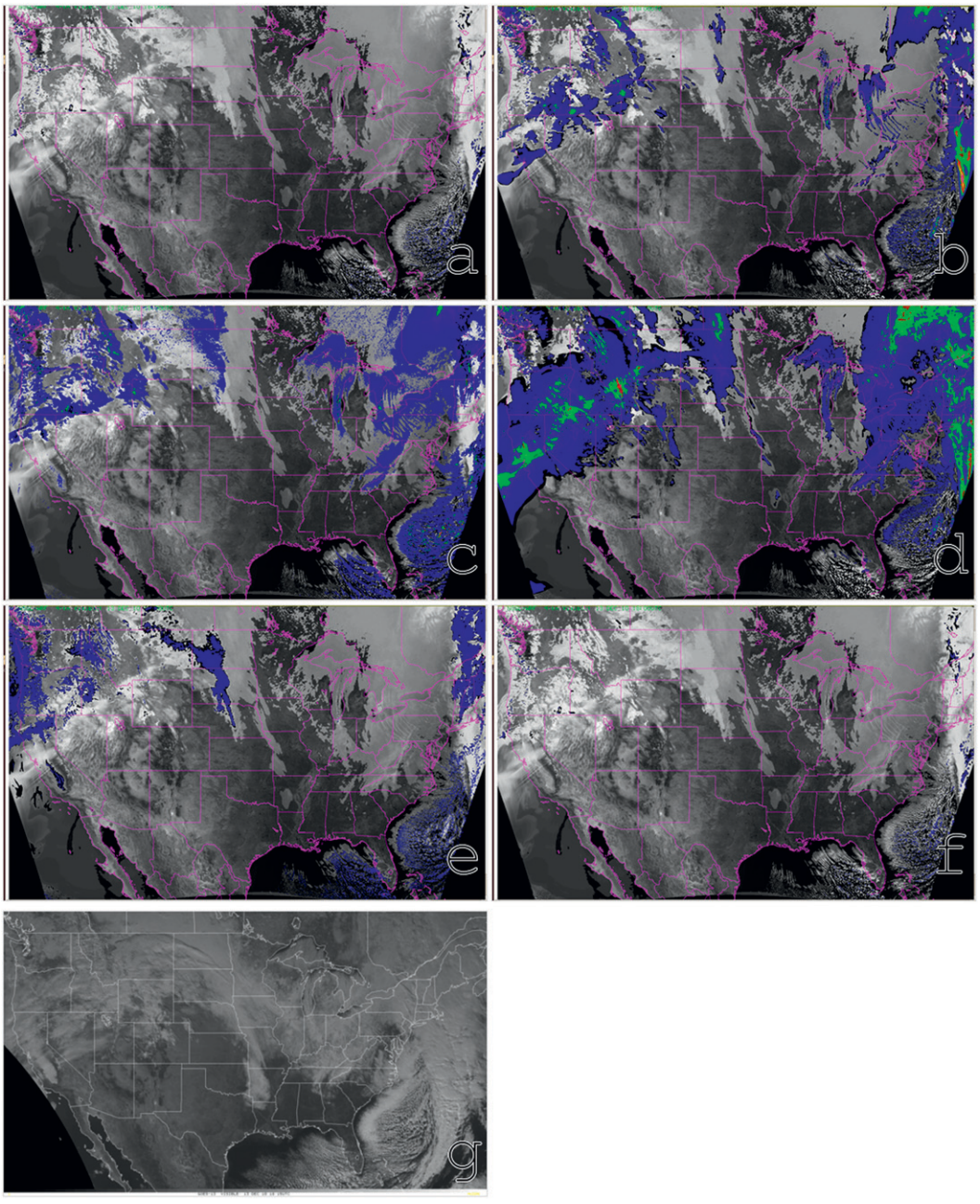

FIG. 5. The 18-h forecast valid at 1800 UTC 13 Dec 2010. Relative values of superimposed quantities (kg m^{-3}) increase from blue to green to red. (a) Visible image for 1800 UTC 13 Dec 2010 simulated using the NN approximation. (b) As in (a), but with the vertically integrated cloud snow content superimposed. (c) As in (a), but with 1-h accumulated precipitation superimposed. (d) As in (a), but with the vertically integrated cloud ice content superimposed. (e) As in (a), but with the vertically integrated cloud water content superimposed. (f) As in (a), but with vertically integrated cloud rainwater content superimposed. (g) Observed *GOES-13* visible satellite image at 1815 UTC 13 Dec 2010.

the previous hour. This option is useful to visualize the microphysical composition of cloud fields being viewed, and in relating the model forecast parameters with each other. An example of the available visualizations on a test dataset is shown in Fig. 4. The output of the forward radiative transfer model on this NSSL-WRF forecast is shown in Fig. 3.

The visible imagery created from the radiative transfer forward model were produced at two different forecast times (1800 and 2200) for comparison with the

neural network version during the NOAA HWT (Clark et al. (2012)) and GOES-R Proving Ground Project in 2010. While the visible imagery from the forward model took hours to compute and were generally available well after the valid time of the forecast, the visible imagery from the neural network approximation were available minutes after the WRF forecasts were produced. It took, on average, 3 min of wall-clock time to generate the simulated visible image from a WRF forecast, with nearly 80% of time used in reading the WRF model output. If the approximation is incorporated into the WRF post-processing itself, where the inputs to the neural network are already in main memory, the computation of visible imagery can be reduced to a few seconds per forecast period.

Example images from an 18-h forecast valid at 1800 UTC 13 December 2010 are shown in Fig. 5. It should be noted that the simulated visible reflectance is reasonable even though wintertime cases were not part of the training dataset. Arctic airflow over the Great Lakes and southeastern coastal waters was occurring at this time. North to south cloud-oriented bands to the south of Lakes Michigan, Huron, and Erie were associated with heavy lake-effect snow squalls. Cloud snow content and surface accumulation are significant in these areas where several centimeters of snow were observed. Parallel cloud bands and cellular clouds offshore of the southeast U.S. and Gulf coasts are evident in the imagery. Given the shallow nature of most of these clouds, they are composed mainly of cloud water without much rainwater. Large areas of thin cloud cover composed mainly of ice surround the snow squalls, and are widespead through an upper-level trough and surface low in the northeast United States, with an upper jet stream from northern California to Montana.

Figure 5g shows an observed visible image from the *GOES-13* (east) geostationary satellite corresponding to the 18-h forecast from the NSSL-WRF shown in Figs. 5a–f. Much of the difference in cloud locations and visual properties between the observed (Fig. 5g) and NN-simulated image (Fig. 5a) can be attributed to forecast error. In general the qualitative structure of the cloud areas are similar, especially the deeper (brighter) clouds with precipitation or high water, ice, snow content, and the shallow convective clouds where cold air is moving over the warmer waters off the Atlantic and Gulf of Mexico coasts. Some of the clear-sky regions in the observed image (U.S. Midwest) appear bright (high albedo) because of snow cover. The snow-covered surface cannot be easily distiguished from cloud cover from the visible image alone, but the distinction is clear in the simulated image since the assumed clear-sky albedo is representative of the summer months.

4. Summary

Although a forward radiative transfer model is capable of providing a depiction of nonprecipitating clouds in a numerical weather prediction model forecast, present-day forward models are too slow to provide timely output for routine weather forecasts. Therefore, an approximation to the behavior of a radiative transfer model on some representative NWP forecasts was created using a neural network. The resulting approximation is very close to the complex radiative transfer model, but has the advantage of being calculable in a small fraction of the time required for the full forward model. This approximation is now carried out routinely in the NOAA HWT and used as routine forecast guidance at the NOAA Storm Prediction Center. Furthermore, the synthetic visible product has been employed extensively as a diagnostic tool in recent HWT research activities, particularly those focusing on convective initiation.

Acknowledgments. The authors are grateful for support from the NOAA High Performance Computing and Communication (HPCC) program, which made this project possible. Funding for the lead author was provided under NOAA–OU Cooperative Agreement NA17RJ1227. We thank Tom Greenwald for his suggestions throughout the project. We also thank Justin Sieglaff for his suggestion to include an analysis of the NN approximation error by reflectance value (Fig. 2).

REFERENCES

Baum, B., P. Yang, A. J. Heymsfield, S. Platnick, M. D. King, Y.-X. Hu, and S. T. Bedka, 2005: Bulk scattering properties for the remote sensing of ice clouds. Part II: Narrowband models. *J. Appl. Meteor.,* **44,** 1896–1911.

Bishop, C., 1995: *Neural Networks for Pattern Recognition*. Oxford University Press, 504 pp.

Clark, A. J., and Coauthors, 2012: An overview of the 2010 Hazardous Weather Testbed Experimental Forecast Program Spring Experiment. *Bull. Amer. Meteor. Soc.,* **93,** 55–74.

Dixon, M., Z. Li, H. Lean, N. Roberts, and S. Ballard, 2009: Impact of data assimilation on forecasting convection over the United Kingdom using a high-resolution version of the Met Office unified model. *Mon. Wea. Rev.,* **137,** 1562–1584.

Feltz, W. F., K. M. Bedka, J. A. Otkin, T. Greenwald, and S. A. Ackerman, 2009: Understanding satellite-observed mountain-wave signatures using high-resolution numerical model data. *Wea. Forecasting,* **24,** 76–86.

Han, Q., Q. Rossow, R. Welch, A. White, and J. Chou, 1995: Validation of satellite retrievals of cloud microphysics and liquid water path using observations from FIRE. *J. Atmos. Sci.,* **52,** 4183–4195.

Heidinger, A., C. O'Dell, R. Bennartz, and T. Greewald, 2006: The successive order-of-interaction radiative transfer model. Part I: Model development. *J. Appl. Meteor. Climatol.,* **45,** 1388–1402.

Heymsfield, A., S. Matrosov, and B. Baum, 2003: Ice water path-optical depth relationships for cirrus and deep stratiform ice cloud layers. *J. Appl. Meteor. Climatol.,* **42,** 1369–1390.

Hong, S., and J.-O. J. Lim, 2006: The WRF single-moment 6-class microphysics scheme. *J. Korean Meteor. Soc.,* **42,** 129–151.

Jakob, C., 1999: Cloud cover in the ECMWF reanalysis. *J. Climate,* **12,** 947–959.

Janjic, Z. I., 1990: The step-mountain coordinate: Physical package. *Mon. Wea. Rev.,* **118,** 1429–1443.

Kain, J. S., and Coauthors, 2008: Some practical considerations regarding horizontal resolution in the first generation of operational convection-allowing NWP. *Wea. Forecasting,* **23,** 931–952.

——, S. Dembek, S. J. Weiss, J. L. Case, J. J. Levit, and R. A. Sobash, 2010a: Monitoring selected fields and phenomena every time step. *Wea. Forecasting,* **25,** 1536–1542.

——, and Coauthors, 2010b: Assessing advances in the assimilation of radar data and other mesoscale observations within a collaborative forecasting–research environment. *Wea. Forecasting,* **25,** 1510–1521.

Koch, S. E., B. Ferrier, M. Stolinga, E. Szoke, S. J. Weiss, and J. S. Kain, 2005: The use of simulated radar reflectivity fields in the diagnosis of mesoscale phenomena from high-resolution WRF model forecasts. Preprints, *11th Conf. on Mesoscale Processes,* Albuquerque, NM, Amer. Meteor. Soc., J4J.7. [Available online at http://ams.confex.com/ams/32Rad11Meso/techprogram/paper_97032.htm.]

Krasnopolsky, V. M., M. Fox-Rabinovitz, H. Tolman, and A. A. Belochitski, 2008: Neural network approach for robust and fast calculation of physical processes in numerical environmental models: Compound parameterization with a quality control of larger errors. *Neural Networks,* **21,** 535–543.

Lakshmanan, V., A. Fritz, T. Smith, K. Hondl, and G. J. Stumpf, 2007: An automated technique to quality control radar reflectivity data. *J. Appl. Meteor.,* **46,** 288–305.

Marzban, C., and G. Stumpf, 1996: A neural network for tornado prediction based on Doppler radar-derived attributes. *J. Appl. Meteor.,* **35,** 617–626.

Otkin, J., and T. Greenwald, 2008: Comparison of WRF model-simulated and MODIS-derived cloud data. *Mon. Wea. Rev.,* **136,** 1957–1970.

——, ——, J. Sieglaff, and H.-L. Huang, 2009: Validation of a large-scale simulated brightness temperature dataset using SEVIRI satellite observations. *J. Appl. Meteor. Climatol.,* **48,** 1613–1626.

Rogers, E., and Coauthors, 2009: The NCEP North American mesoscale modeling system: Recent changes and future plans. Preprints, *23rd Conf. on Weather Analysis and Forecasting/19th Conf. on Numerical Weather Predicition,* Omaha, NE, Amer. Meteor. Soc., 2A.4. [Available online at http://ams.confex.com/ams/pdfpapers/154114.pdf.]

Sayer, A., G. Thomas, and R. Grainger, 2010: A sea surface reflectance model for AATSR and application to aerosol retrievals. *Atmos. Meas. Technol.,* **44,** 1896–1911.

Skamarock, W., J. Klemp, J. Dudhia, D. Gill, D. Barker, W. Wang, and J. Powers, 2005: A description of the Advanced Research WRF version 2. National Center for Atmospheric Research Tech. Rep. NCAR/TN-468-STR, 88 pp. [Available from UCAR Communications, P.O. Box 3000, Boulder, CO 80307.]

Sundqvist, H., E. Berge, and J. E. Kristjnsson, 1989: Condensation and cloud parameterization studies with a mesoscale numerical weather prediction model. *Mon. Wea. Rev.,* **117,** 1641–1657.

Teixeira, J., and T. Hogan, 2002: Boundary layer clouds in a global atmospheric model: Simple cloud cover parameterizations. *J. Climate,* **15,** 1261–1271.

Venkatesan, C., S. Raskar, S. Tambe, B. Kulkarni, and R. Keshavamurty, 1997: Prediction of all India summer monsoon rainfall using error-back-propagation neural networks. *Meteor. Atmos. Phys.,* **62,** 225–240.

Weisman, M., C. Davis, W. Wang, K. Manning, and J. Klemp, 2008: Experiences with 0–36-h explicit convective forecasts with the WRF-ARW model. *Wea. Forecasting,* **23,** 407–437.

Weiss, S. J., M. E. Pyle, Z. Janjic, D. R. Bright, J. S. Kain, and G. J. DiMego, 2008: The operational high-resolution window WRF model runs at NCEP: Advantages of multiple model runs for severe convective weather forecasting. Preprints, *24th Conf. on Severe Local Storms,* Savannah, GA, Amer. Meteor. Soc., P10.8. [Available online at http://ams.confex.com/ams/24SLS/techprogram/paper_142192.htm.]